ChemSusChem
Chemistry–Sustainability–Energy–Materials

Chemistry Europe
European Chemical Societies Publishing

Title: Nanoconfinement-Driven Energy-Efficient CO2 Capture and Release at High Pressures on a Unique Large-Pore Mesoporous Carbon

Authors: Laszlo Szabo, Mizuki Inoue, Yurina Sekine, Ryuhei Motokawa, Yusuke Matsumoto, Thi Thi Nge, Edhuan Ismail, Izumi Ichinose, and Tatsuhiko Yamada

To be cited as: *ChemSusChem* **2025**, e202402034

Link to VoR: https://doi.org/10.1002/cssc.202402034

WILEY-VCH

10.1002/cssc.202402034

Nanoconfinement-Driven Energy-Efficient CO_2 Capture and Release at High Pressures on a Unique Large-Pore Mesoporous Carbon

László Szabó, [a] Mizuki Inoue,[b] Yurina Sekine,[c,d] Ryuhei Motokawa,[d] Yusuke Matsumoto,[a] Thi Thi Nge,[a] Edhuan Ismail,[b] Izumi Ichinose,* [b] Tatsuhiko Yamada * [a]*

[a] Center for Advanced Materials, Forestry and Forest Products Research Institute (FFPRI), 1 Matsunosato, Tsukuba, Ibaraki 305-8687, Japan

[b] Research Center for Macromolecules and Biomaterials, National Institute for Materials Science (NIMS), 1-1 Namiki, Tsukuba, Ibaraki 305-0044, Japan

[c] Promotion Office, Japan Atomic Energy Agency (JAEA), Tokai, Naka-gun, Ibaraki 319-1195, Japan

[d] Materials Sciences Research Center, JAEA, Tokai, Naka-gun, Ibaraki 319-1195, Japan

***Corresponding authors**

E-mail addresses: szabo@affrc.go.jp (L. Szabó); ichinose.izumi@nims.go.jp (I. Ichinose); yamadat@affrc.go.jp (T. Yamada)

Abstract

Although microporous carbons can perform well for CO_2 separations under high pressure conditions, their energy-demanding regeneration may render them a less attractive material option. Here, we developed a large-pore mesoporous carbon with pore sizes centered around 20-30 nm using a templated technical lignin. During the soft-templating process, unique cylindrical supramolecular assemblies form from the copolymer template. This peculiar nanostructuring takes place due to the presence of polyethylene glycol (PEG) segments on both the Pluronic® template and the PEG-grafted lignin derivative (glycol lignin). A large increase in CO_2 uptake occurs on the resulting large-pore mesoporous carbon at 270 K close to the saturation pressure (3.2 MPa), owing to capillary condensation. This phenomenon enables a CO_2/CH_4 selectivity (S_{CO_2/CH_4}, mol/mol) of 3.7 at 270 K and 3.1 MPa absolute pressure, and a swift pressure swing regeneration process with desorbed CO_2 per unit pressure far outperforming a benchmark activated carbon (*i.e.*, notably rapid decrease in the amount of adsorbed CO_2 with decreasing pressure). We propose large-pore mesoporous carbons as a novel family of CO_2 capture adsorbents, based on the phase-transition behavior shift of CO_2 in the nanoconfined environment. This novel material concept may open new horizons for physisorptive CO_2 separations with energy-efficient regeneration options.

Keywords: carbon dioxide fixation, lignin, mesoporous carbon, regeneration, template synthesis

1. Introduction

Carbon capture, utilization and storage technologies are at the heart of climate change mitigation policies aimed at decreasing the concentration of greenhouse gases in the atmosphere.[1,2] Nevertheless, already at the CO_2 capture stage, existing methods are considered costly and energy-intensive, compromising the economic feasibility and overall environmental benefit of these technologies.[3,4] It has been extensively recognized that the physicochemical properties of the sorbent have crucial impact on the capital and operating costs of CO_2 removal processes.[1] Amine scrubbing for example, a mature technology to capture CO_2, involves a chemisorption process using aqueous monoethanolamine (MEA).[5] The energy intensive regeneration step is seen as a major obstacle to the widespread implementation of this process, along with other issues, such as the thermal and oxidative degradation of MEA under operating conditions, together with the corrosive nature of the media.[6] Therefore, great efforts have been directed towards the development of novel low-cost materials that can capture and release CO_2 in an energy-efficient and cyclable manner.[7,8]

Solid-based physisorptive CO_2 capture processes have come to the fore, providing structurally more stable systems with less energy intensive regeneration steps, on account of the lower enthalpy of physisorption compared to chemisorption.[9-11] Nanoporous carbons provide tunable platforms within this group for their pore structure can be tailored, enabling the realization of energetically more favorable regeneration steps inasmuch as the enthalpy of adsorption is generally smaller in mesopores (2 nm < d_p < 50 nm) compared to micropores (d_p < 2 nm). It has also been reported that an interconnected micro-mesoporous carbon material with less amount of micropores and surface area can in fact adsorb larger amount of CO_2 at ambient temperature and 0.5/1 MPa pressure or at 308 K and ambient pressure, compared to a fully microporous carbon, highlighting the importance of tailored hierarchical pore designs that can enhance molecular transport.[12] In addition, these structurally stable materials may be the adsorbents of choice under extreme operating conditions. For example, natural gas streams may initially experience pressures as high as 120 MPa.[13,14] There has been an increasing interest in designing materials for removing CO_2 from natural gases, driven by various technological/economical/environmental disadvantages connected to CO_2 residues, together with projected increasing worldwide demand.[15,16]

Among the physisorptive CO_2 capture technologies, pressure swing adsorption (PSA) has been recognized as a superior process offering rapid adsorption/desorption cycles (within minutes or even seconds), simple operation, low costs and energy requirements compared to the more energy-intense temperature swing process.[17,18] A low temperature PSA process offers untapped opportunities for CO_2 separations within a vastly uncharted thermodynamic space compared to the common ambient temperature operation.[15] At low temperatures, adsorption capacities and differences in the rate of adsorption between gases can be greater, and the adsorbent may also behave differently under such conditions. In liquid natural gas (LNG) plants for example, high feed gas pressures and low temperature streams are readily available. Thus, a refrigerant loop could be easily used to cool down the PSA feed gas. Once the captured CO_2 is recovered, it is compressed to a supercritical fluid/liquid state (critical point at 7.4 MPa and 304.15 K).[1] Except pipeline transportation that can occur above the critical pressure but below the critical temperature, CO_2 is converted to a cryogenic liquid (*e.g.*, transport by ship under a pressure of 0.65 MPa at a temperature of 222 K).[19] Therefore, a low temperature PSA process can bring about lower overall energy penalty compared to technologies operating with a high-temperature regeneration process.

Micro-mesoporous carbons have shown excellent CO_2 adsorption performance compared to conventional microporous activated carbons as reported in several works,[12,20-22] both in the atmospheric and high-pressure regimes. Such hierarchical pore design allows for an improved molecular transport within the material under atmospheric conditions, while mesopore filling facilitates CO_2 capture at higher pressures. Nevertheless, our understanding is still limited on the behavior of CO_2 in mesopores of increasing sizes in the high-pressure regime, especially close to the saturation pressure where pore condensation may facilitate large uptake of CO_2. Vorokhta et al.[20] prepared an ordered mesoporous carbon with large 14-15 nm spherical pores. This material not only outperformed various other nanoporous carbons close to the saturation pressure (including ordered mesoporous carbons with smaller pore sizes of about 4 nm),[23,24] but also exhibited an exceptional steep CO_2 uptake profile, indicating the possibility of a more energy-efficient (*e.g.*, pressure swing) regeneration process. The phase behavior of CO_2, confined in mesopores, was studied in detail revealing distinct pore condensation phenomena in mesopores of smaller, and of larger sizes at high pressures and low temperatures.[25]

Mesoporous carbons with controlled pore size and spatial arrangement can be readily designed through various templating strategies.[26-28] Among the available methods, soft-templating provides a direct way to these materials with less waste generation compared to tedious hard templating (or nanocasting) methods, and therefore, it has been identified as a more sustainable synthesis route.[29] In these systems, structure-directing surfactants self-assemble into meso-sized domains with various symmetries; mesoporous carbons with pore sizes less than 10 nm can be usually obtained using typical commercially available nonionic amphiphilic block copolymer surfactants (poloxamers or Pluronics®). Mesoporous carbons with larger pore sizes are widely referred to as large-pore mesoporous carbons. Their fabrication is more challenging, particularly if well-structured (ordered) systems are desired, as this usually involves the initial synthesis of larger tailor-made amphiphilic block copolymer templates.[28,30,31] It should be noted that soft-templating methods are generally based on phenolic resins as carbon precursors.[26-28]

In realizing the future potential of various carbon nanoarchitectures for sustainable technologies, synthesis methods have been critically discussed focusing on biosourced building blocks with lower carbon footprint and cost compared to petroleum-based phenolic alternatives.[29,32,33] Lignin, the most abundant aromatic biopolymer available on Earth, has emerged as a leading candidate for the large-scale implementation of biosourced nanocarbons into high-end products and technologies.[34-37] Nevertheless, it has proved difficult to use technical lignins alone (the industrially available product after extracting native lignin from biomass) for soft-templating that was originally developed on phenolic resins.[38-42] This issue can be attributed to the lack of cooperative interactions between the surfactant and lignin molecules, which is known to be an essential requirement for the self-assembly when phenolic resins are used.[26] The reasons may lie in the branched and larger structure of lignin and/or the absence of sterically easily accessible functional groups, restricting self-organization and the development of secondary interactions, *e.g.*, hydrogen bonding for phenolics. In order to overcome these challenges, either phloroglucinol/lignin blends have been used,[39,40] or a metal coordinated self-assembly strategy has been applied in previous works.[41,42] It should be noted that mimosa tannin, a natural polyphenolic compound, could be converted into ordered mesoporous carbons in pioneering works, via environmentally benign water-based procedures using Pluronic® 127 without the need of a crosslinker.[43,44]

Here, we use a functionalized technical lignin, coined as glycol lignin, prepared through an acid-catalyzed polyethylene glycol (PEG) solvolysis process.[45] Glycol lignin has the same repeating ethylene oxide structural unit that can be found in the hydrophilic segments of poloxamers, the typical surfactants for soft- templating methods (Fig. 1). In this work, we shed light on the formation of unique supramolecular self-assemblies in a technical lignin/soft-template system for the first time. We also discuss on the exceptional properties of the forming large-pore mesoporous carbon for CO_2 capture application at high pressures and low temperatures. We believe that our work will facilitate further efforts for the realization of lignin-based advanced carbon nanoarchitectures, and open the gates for the development of tailored mesoporous structures for cost-effective CO_2 capture applications.

2. Experimental section

2.1. Materials

Glycol lignin was obtained from Japanese cedar (*Cryptomeria japonica*) through an acid-catalyzed PEG solvolysis process developed at the Forestry and Forest Products Research Institute (Japan). The delignification process, the structure of glycol lignin and its thermal properties have been described in detail in our previous works.[45-47] The glycol lignin used here was produced with PEG having an average molecular weight of 400 g mol^{-1}. For comparison, the glycol lignin sample has a Klason lignin content of ~82% (*i.e.*, about 18 wt% of glycol lignin consists of polyethylene glycol units), and a weight average molecular weight of 5540 g mol^{-1} with a polydispersity index of 3.72 (as determined through size exclusion chromatography (SEC) experiments).[45-47]

Glycol lignin samples were dried in a vacuum drying oven (Eyela Vacuum Oven VOS-301SD; Tokyo Rikakikai, Tokyo, Japan) at room temperature, and kept in desiccators before the experiments (moisture content was generally below 1 wt%; determined using an HS153 Moisture Analyzer from Mettler Toledo, Columbus, OH, USA).

The nonionic surfactant triblock copolymer Pluronic® F-127 (Catalogue No. P2443) and 40 wt% aqueous glyoxal solution (Catalogue No. 128465) for the soft-templating method were purchased from Sigma Aldrich (St. Louis, MO, USA). Acetone (Catalogue

No. 016-00346) was provided by Fujifilm Wako Pure Chemical Corporation (Osaka, Japan). An Eyela Still Ace SA-2100E1 (Tokyo Rikakikai, Tokyo, Japan) water purification system provided deionized water for the experiments.

Shirasagi® WH5C, a granular coal-based microporous activated carbon, was purchased from Osaka Gas Chemicals Co., Ltd. (Osaka, Japan).

2.2. Soft-templating process

The main synthesis steps are highlighted with some illustrations in Fig. 1. In a typical procedure, 2 g Pluronic® F-127 was dissolved in 25 mL acetone/water (4/1 v/v) mixed solvent system at room temperature within 1 hour in closed vials. 1 g glycol lignin was then added to the sample. The solution was stirred for 1 hour, followed by the addition of 1 mL 40 wt% aqueous glyoxal solution (for cross-linked samples). The resulting solution was stirred for 10 min, and then poured into polytetrafluoroethylene (PTFE) evaporating dishes (Cowie, Middlesbrough, UK). The evaporating dishes were placed under the fume hood for 3 days, followed by a curing step in an oven (ETTAS EOP-300B; AS ONE Corporation, Osaka, Japan) at 85 ºC for 3 days. The resulting sample is designated as "F/Gl/C 2/1/1" indicating the amount of surfactant (F)/glycol lignin (Gl)/aqueous glyoxal solution (C) added to the 25 mL mixed solvent according to the above procedure. For example, F/Gl/C 1/1/1 was prepared using 1 g Pluronic® F-127, 1 g glycol lignin, and 1 mL crosslinker following the above procedures. Samples with other composition follow this designation rule throughout the manuscript.

2.3. Carbonization process

Carbonization experiments were done in a tube furnace under constant N_2 flow (200 mL min^{-1}; 99.995% purity). The tube furnace setup consisted of an ARF-800-50KC type furnace connected to an AMF-9P-III type controller unit from Asahi Rika Seisakusho Co., Ltd. (ASH; Chiba, Japan). The temperature program comprised the following steps. First, the furnace was heated to 105 ºC in 30 min, followed by an isothermal step at 105 ºC for 30 min. Next, the furnace was heated to 800 ºC with 5 ºC min^{-1} heating rate, and thereafter, the temperature was kept at 800 ºC for 1 h. At that point, the program was terminated leaving the system to cool down to ambient temperature.

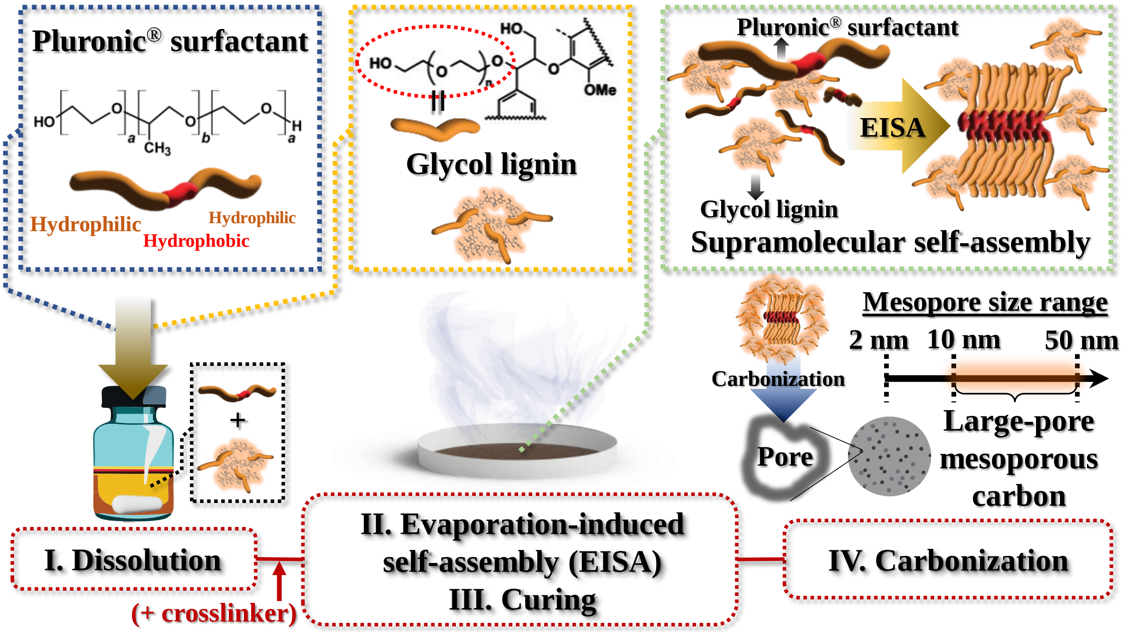

Fig. 1. Schematic representation on the preparation of the large-pore mesoporous carbon through the formation of supramolecular surfactant self-assemblies in a glycol lignin matrix.

2.4. Characterization

Thermogravimetric analysis (TGA) was performed under N_2 atmosphere using a TGA Q500 apparatus from TA Instruments (New Castle, DE, USA). The following temperature program was applied: The temperature was increased first to 105 ºC at a rate of 10 ºC min^{-1}, followed by an isothermal process for 20 min to remove residual water. Thereafter, a heating ramp was applied at a rate of 10 ºC min^{-1} to 850 ºC as a last step. TGA experiments were done under N_2 atmosphere using a flow rate of 60 mL min^{-1} for the furnace chamber containing the sample.

Attenuated total reflectance Fourier-transformed infrared spectroscopy (ATR-FTIR) was done using a Nicolet iS50 spectrometer equipped with a single-bounce diamond crystal ATR accessory (Thermo Fisher Scientific Inc., Waltham, MA, USA). Spectra were recorded with a resolution of 4 cm^{-1}. 32 scans were collected and averaged. ATR correction and baseline-adjustment were done using the Thermo Scientific OMNIC software. Samples were dried in a vacuum drying oven at room temperature (Eyela Vacuum Oven VOS-301SD; Tokyo Rikakikai, Tokyo, Japan) prior to the analysis.

N_2 adsorption-desorption experiments were carried out at 77 K using a BELSORP-mini II specific surface area and pore size analyzer (MicrotracBEL Co., Osaka, Japan). Samples were pretreated at 120 ºC overnight in a BELPREP VAC II vacuum degasser. The BELMaster^{TM} software was used for data analysis. The specific surface area was determined using the Brunauer-Emmett-Teller (BET) method.[48] The Barrett-Joyner-Halenda (BJH) model was applied to calculate the mesopore size distribution either from the adsorption or desorption branch of the isotherm.[49] The micropore volume was calculated using the *t*-plot method according to Lippens and de Boer, and the total pore volume was determined from the amount of N_2 gas adsorbed at a relative pressure (p/p_0) of 0.99 following the Gurvich rule (given that the isotherm exhibits a plateau).[49,50] The mesopore volume can be then obtained by subtracting the micropore volume from the total pore volume.

Small-angle neutron scattering (SANS) experiments were conducted using the SANS-J diffractometer installed at the cold neutron guide (C3-2) of the research reactor (JRR-3) at JAEA in Tokai, Japan.[51,52] 2D scattering profiles were recorded with sample-to-detector distances of 2 m and 10 m, covering a magnitude of scattering vector (q) from 0.025 nm^{-1} to 2 nm^{-1}, where $q = (4\pi/\lambda)\sin(\theta/2)$, with λ (= 0.65 nm) and θ being the wavelength of incident neutrons and scattering angle, respectively. 2D images were azimuthally averaged to obtain 1D SANS profiles. The 1D SANS profiles were subjected to normalization with sample transmittance, and background correction was performed by subtracting the SANS profile of the empty quartz cell. SANS data recorded at different sample-to-detector distances were combined using the Irena package written for Igor Pro.[53] Quantitative data analysis, for obtaining pair distance distribution functions, and for fitting the unified model developed by Beaucage,[54-56] were also conducted within the Irena package. The SasView software was used to obtain best-fit theoretical scattering curves using the models as described later.[57]

Microscopic structure of the samples at nano-length scales was observed using a Hitachi S-4800 field emission scanning electron microscope (FE-SEM; Hitachi Ltd., Tokyo, Japan).

2.5. High-pressure gas adsorption experiments

High-pressure gas adsorption experiments were conducted on a BELSORP HP (MicrotracBEL Co., Osaka, Japan) volumetric device. Pretreatment was done at 200 ºC for 5 h under vacuum prior to the experiments. Temperature was controlled using a chiller bath (LTB-250A type; AS ONE Corporation, Osaka, Japan). Gas adsorption data were recorded with an equilibrium time of 300 sec. CO_2 and CH_4 gas with a purity of 99.995% and 99.999%, respectively, were used throughout the experiments. Isosteric heat of adsorption (Q_{st}) was determined from adsorption isotherms obtained at three different temperatures (243, 253 and 263 K) using the Clausius-Clapeyron equation.[13] CO_2/CH_4 gas selectivities (S_{CO_2/CH_4}, mol/mol) were calculated for equimolar CO_2/CH_4 mixtures. The molar loadings for the binary mixture were estimated from single gas adsorption isotherms, similar to the ideal adsorption solution theory (IAST) according to others.[58-60] Due to the lack of an adsorption model that could describe the multilayer adsorption process with the steep pore condensation step, a polynomial fit that captured best the shape of the isotherms helped estimating the adsorbed amount at the chosen absolute pressure.

3. Results and discussion

Glycol lignin and the Pluronic® F-127 surfactant (a typical structure directing agent for soft-templating) share the same ethylene oxide repeating structural motif (Fig. 1), which may facilitate the development of secondary interactions that seem to be absent when organosolv or kraft lignin is used for soft-templating.[38-40] Such cooperative interaction is known to be an essential requirement for surfactant self-assemblies to form.[29] We were able to readily dissolve both glycol lignin and the block copolymer amphiphilic surfactant in the same mixed acetone/water solvent system (4/1 v/v), enabling us to prepare homogenous polymer composites following an evaporation-induced self-assembly (EISA) process. During the EISA process, surfactant molecules assemble into supramolecular structures while the solvent slowly evaporates (Fig. 1).[61] For the mesoporous carbon to form upon carbonization at high temperature (800 ºC here), these supramolecular structures need to be physically trapped in the matrix; this can be achieved by cross-linking the system. We applied glyoxal as cross-linker according to previous studies,[39,40] which is a less harmful alternative to formaldehyde.[29] Glycol lignin can be cross-linked similarly to other technical lignins as we confirmed by ATR-FTIR measurements (Fig. S1). A detailed explanation on these results, together with a discussion on the glyoxalation reaction can be found in the Supporting Information (page S2-S3).

A range of polymer composites were prepared by fixing the amount of glycol lignin (Gl) and the cross-linker (C), while systematically increasing the amount of the surfactant (F; composites are given the F/Gl/C designation accordingly) in the system. The prepared composite samples were subjected to a carbonization step at 800 ºC. Pluronic® F-127 is a sacrificial, pore forming component since it fully decomposes upon heating above 400 ºC (Fig. S3), meanwhile glycol lignin is converted to a graphitic-like turbostratic carbon above high temperatures. A detailed explanation and discussion on the thermal behavior of the composite can be found in the Supporting Information (page S4-S6).

3.1. Pore structure analysis through N_2 adsorption-desorption experiments

The pore structure of the carbonaceous residues after the carbonization treatment was studied first through N_2 adsorption-desorption experiments (Fig. 2). The carbon sample obtained from glycol lignin exhibits a type I isotherm with a large uptake of N_2 in the low relative pressure range (Fig. 2A), characteristic for microporous carbons.[50] A specific surface area of 471 $m^2 g^{-1}$, and a micropore volume of 0.19 $cm^3 g^{-1}$ were calculated from the isotherm. Our results indicate that microporosity develops largely owing to the decomposition of PEG side chains below 400 ºC (see the TGA results and related discussion, Supporting Information page S4-S6). Technical lignins do not generally yield microporous carbons with such high surface area and pore volume (*e.g.*, a specific surface area of ~80 $m^2 g^{-1}$ was reported for beechwood derived organosolv lignin).[39]

Following the addition of surfactant to the system, mesopores are generated in the structure with growing amount as the surfactant concentration increases (Table S1 lists the surface areas and pore volumes derived from the isotherms); the presence of mesopores are clearly indicated by the capillary condensation step with a well-defined plateau at high relative pressures (Fig. 2A; except for sample F/Gl/C 2.5/1/1). Thus, micro-mesoporous carbons are generated with isotherms exhibiting both Type I and Type IV features.[50] Furthermore, a hysteresis loop is present (for samples containing larger amount of surfactant than F/Gl/C 1/1/1) in connection to the capillary condensation step.

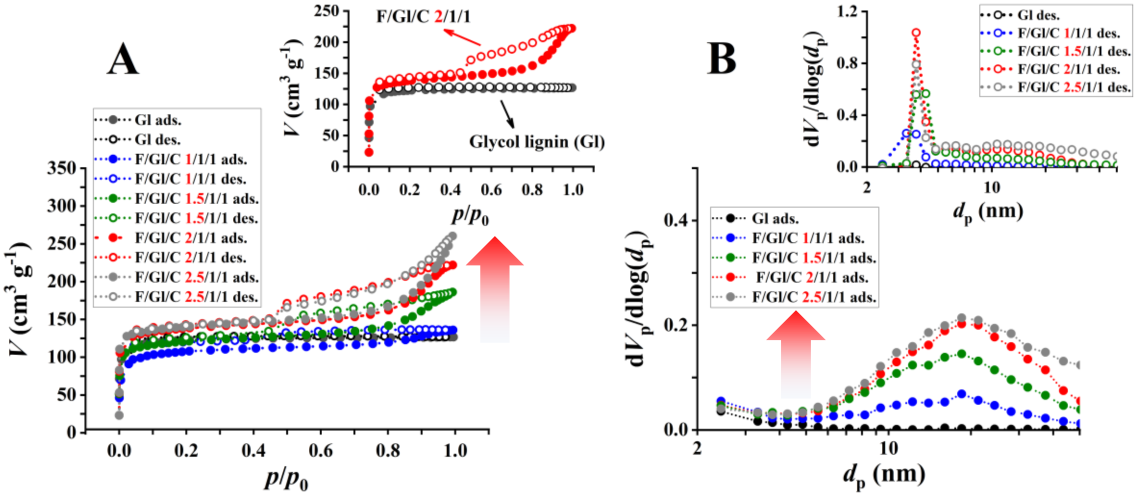

Fig. 2. (A) N_2 adsorption-desorption isotherms measured on carbonized glycol lignin (Gl) and cross-linked, carbonized Gl samples containing increasing amount of Pluronic® F-127 (F, from 1-2.5 g). Inset highlights the micro-mesoporous sample chosen for the CO_2 adsorption experiments. (B) The corresponding pore size distribution curves derived using either the adsorption or (inset) the desorption branch of the isotherm.

The closure point is located at around the relative pressure of 0.42, as typically observed for numerous nitrogen hysteresis loops.[49] The hysteresis loop in Fig. 2A resembles an H2(b) type loop according to IUPAC classification, suggesting a complex pore network structure.[50,62] The lower closure point of the hysteresis loop in such cases may be associated with artifacts, such as cavitation induced evaporation (often called the “tensile strength effect”),[63] and/or with pore-blocking/percolation for “ink-bottle” type pore network.[49,50,62] On account of these issues, the adsorption branch may provide a more reliable semi-quantitative pore size distribution, keeping in mind the metastable nature of the adsorbed multilayer (*i.e.*, no thermodynamic equilibrium).[62]

Fig. 2B shows the pore size (or volume) distribution derived from the adsorption branch using the BJH method (pore size (area) distribution is given in Fig. S4). A wide pore size distribution can be noticed that peaks at ~20-30 nm, indicating the formation of a large-pore mesoporous carbon. As we outlined earlier, soft-templating methods based on Pluronic® surfactants usually afford mesoporous carbons with pore sizes below 10 nm, together with the possibility of ordered pore arrangements featuring various symmetries (*e.g.*, hexagonal cubic *p*6*m*, body-centered cubic *Im*3*m*, *etc.*).[29] This also applies to soft-templating methods based on technical lignins and Pluronic® F-127. For example, Herau et al.[39] obtained an ordered mesoporous carbon with ~4 nm pore diameter from phloroglucinol/organosolv lignin blends. In another work, Wang et al.[41] realized ordered mesoporous carbons with similar pore sizes using organosolv lignin mixed with metal salts (a metal-coordinated self-assembly process). Kraft lignin afforded largely disordered, micro-meso-macroporous structures after soft-templating.[38] Formation of a large-pore mesoporous carbon from a technical lignin in our system is a quite unique phenomenon. This must be connected to the occurrence of markedly different supramolecular assemblies compared to previous reports, owing to distinct interactions between the surfactant and glycol lignin molecules, as it will be explained later (see the SANS analysis part). Preparation of large-pore mesoporous carbons is usually challenging, since it involves the laborious synthesis of larger block copolymers which are usually less soluble in the soft-templating solvent system, among other issues.[30,31,40] For comparison, we show the pore size distribution obtained from the desorption branch of the isotherms in Fig. 2B inset, which contains the typical artifact with a peak around 4 nm. It will be clear later that this is not the case here.

It should be noted that microscopic approaches, such as the non-local density functional theory (NLDFT) or quenched solid DFT (QSDFT) models are known to better describe the mesopore filling and hysteresis process, compared to methods applying the Kelvin equation (such as the BJH theory) that is based on macroscopic thermodynamic assumptions.[49,50] Thus, when the DFT kernel is consistent with the nanoporous system, microscopic models can provide a more precise pore size analysis. We would also like to point out that scanning of the hysteresis loop can provide additional information on pore connectivity,[64] this method has been demonstrated on model disordered/ordered mesoporous carbons.[65] In a recent work, hierarchy-connectivity factor was introduced by Castro-Gutiérrez et al.,[66] a valuable approach to characterize pore networks. The results of our hysteresis scanning experiments can be seen in Fig. S5. The hysteresis loop retains similar shape when the pores are partially filled (see the loop closing at 0.92 p/p_0). This result indicates that evaporation from certain pores are not affected by the state of adjacent pores, consistent with the independent pore model.[64] In such pore system, desorption can take place by cavitation and not by percolation/pore blocking. It has been suggested that cavitation occurs in pore networks with H2 type loops if the width of the pore neck is below a critical size (5 nm).[65] We performed a detailed SANS analysis as an independent method to aid our further understanding on the pore structure (*vide infra*).

By increasing the amount of the surfactant in the system, we have also realized that at a certain composition, the plateau at high relative pressures disappears (sample F/Gl/C 2.5/1/1, see Fig. 2A). We believe that such composition contains “excessive” amount of surfactant, leading to the collapse of the mesoporous network. Hence, we considered the composition F/Gl/C 2/1/1 optimal for obtaining a micro-mesoporous material to study CO_2 adsorption, as we will discuss later. For this sample, a specific surface area of 533 m^2 g^{-1}, a micropore volume of 0.19 cm^3 g^{-1}, and a mesopore volume of 0.15 cm^3 g^{-1} were derived from the isotherm (Table S1). We also tried the soft-templating process without using cross-linker. In this case, mesopores could not be obtained, a macroporous material formed instead (Fig. S6). The importance of the cross-linker is well known from other studies, for it is essential to “lock” or “trap” the supramolecular assemblies within the precursor matrix due to the thermal instability of the micelles,[67] or in our case probably of some other type of surfactant supramolecular structures (see later).

3.2. Microstructural analysis through SANS

Fig. 3A shows the SANS profile of the cross-linked glycol lignin/Pluronic® F-127 surfactant composite film obtained after the EISA process. A well-defined peak was observed with a maximum at $q \approx 0.44$ nm^{-1}, together with a less prevalent broad feature between 0.1 and 0.3 nm^{-1}. For this part of the SANS profile, the scattering intensity, $I(q)$, may be expressed in terms of a form factor, $P(q)$, representing the shape and size of the scattering objects due to intraparticle interferences, and of a structure factor, $S(q)$, describing correlations between scattering domains owing to interparticle interferences, according to the following equation (1):[68]

$$I(q) = A\big(P(q)S(q)\big) + I(q)_{bck} \tag{1}$$

where A is a proportionality constant, and $I(q)_{\mathrm{bck}}$ is the background. This expression will be used later for fitting model to the data, and may help the quantitative understanding of the scattering profile at this point. Thus, the features of the SANS profile at large q values can be related to the geometric properties of the objects and/or possible correlations between these scatterers, for example to the average Bragg-like spacing between scattering domains (d-spacing, where $d = 2\pi/q$). The scattering intensity at $q \leq 0.1$ nm^{-1}

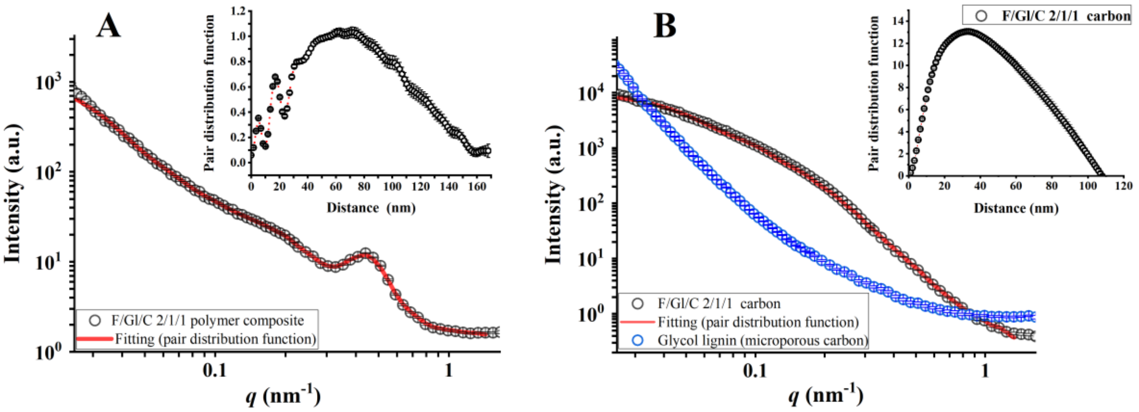

Fig. 3. (A) SANS profile recorded on a polymer composite sample after soft-templating (F/Gl/C 2/1/1), with inset showing the pair distance distribution function based on the fitting. (B) SANS profiles of the carbonized glycol lignin (microporous) sample and the micro-mesoporous carbon (F/Gl/C 2/1/1) with inset depicting the pair distance distribution function derived from fitting to the latter data.

varied in accordance with power law scattering, *i.e.*, $I(q) \sim q^{-\alpha}$, where the exponent, α, was approximately 2.1 corresponding to the mass fractal dimension due to the presence of supramolecular aggregates originating from the block copolymer template (Fig. S7). The pair distance distribution function, $g(r)$, calculated in the q range of ~0.026-1.43 nm^{-1}, is shown in Fig. 3A inset, indicating correlation distances between the scatterers. We can identify peaks at 5 nm and 17 nm, followed by a broad peak (centered around 70 nm) with increasing distance. These distances may be associated with specific dimensions of the scattering domains.

Pluronic® F-127 molecules organize into core-shell spherical micelles above the critical micelle concentration (CMC) and temperature in aqueous solution, with their hydrophilic segments (ethylene oxide units) facing outwards, and their hydrophobic part (propylene oxide units) forming the core. The size of these micelles was studied at low copolymer concentrations via light scattering experiments, revealing a hydrodynamic radius of about 12 nm (at 25 ºC).[69] At sufficiently high polymer concentrations (*e.g.*, above 15 wt%, ~28 ºC < $T \leq$ ~45 ºC),[70] the micelles pack into ordered structures leading to a polymeric micellar macrolattice (lyotropic liquid crystalline phase) with gel-like structure.[69-73] SANS analysis in this gel-like region provided information on the size of the micellar core radius as being around 4-5 nm, and indicated about 60-66 aggregates.[69]

The SANS profiles recorded on this gel-like material consist of a small peak at large q values due to intraparticle interference (from which the hydrophobic core radius is obtained), along with larger peaks at smaller q values which are assigned to interparticle interferences on account of the long-range ordering of the micelles.[69-72] Similar ordered micellar models have been proposed by others under certain conditions for lignin/Pluronic® F-127 solid composites after the EISA process, as suggested indirectly by the formation of an ordered mesoporous carbon upon the carbonization process.[39-42] Nevertheless, the scattering profile that we obtained for the glycol lignin/Pluronic® F-127 system (Fig. 3A) does not indicate similar level of long-range ordering, and we believe that such scattering pattern does not align with a spherical micelle or worm-like model either. Instead, we propose that cylindrical lamellar structures may be present, since we could fit such model within the 0.1-1 nm^{-1} q range (see Fig. S7). The model yielded a core thickness of ~5 nm, a layer thickness of ~8 nm, and a disc radius of ~7 nm (the proposed structure is depicted in Fig. 4). In this model, the stacking number was adjusted to 1, meaning that the SANS profile could be best fit solely by the form factor $P(q)$ in equation (1) without including the structure factor $S(q)$. It follows that long-range ordering does not take place between the objects, *i.e.*, these cylindrical structures are randomly oriented and distributed in the matrix. Nevertheless, stacking may occur, albeit the scattering profile does not indicate appreciable amount of stacked structures. Based on the above considerations, an illustration representing our model for this system is shown in Fig. 4. In other systems, core-shell spherical micelles form in order to minimize surface area and well cover the hydrophobic core. We believe that glycol lignin as a matrix can better accommodate the surfactant molecules on account of secondary interactions between the hydrophilic polyethylene oxide moieties present both on glycol lignin and on the copolymer surfactant molecules, leading to the formation of cylindrical surfactant self-assemblies. Such nanostructuration is distinct from those that occur in phenolic resin/Pluronic® surfactant or other lignin/Pluronic® surfactant systems.

In respect to the neutron scattering length densities (SLD) of the components, lignin is a more powerful scatterer with an SLD of 2.64×10^{10} cm^{-2},[74] compared to the ethylene oxide (0.67×10^{10} cm^{-2}) and propylene oxide (0.34×10^{10} cm^{-2}) units,[75] indicating a good contrast between the lignin matrix and the self-assembled structures. For comparison, the neutron SLD for D_2O, a common agent to improve contrast, is

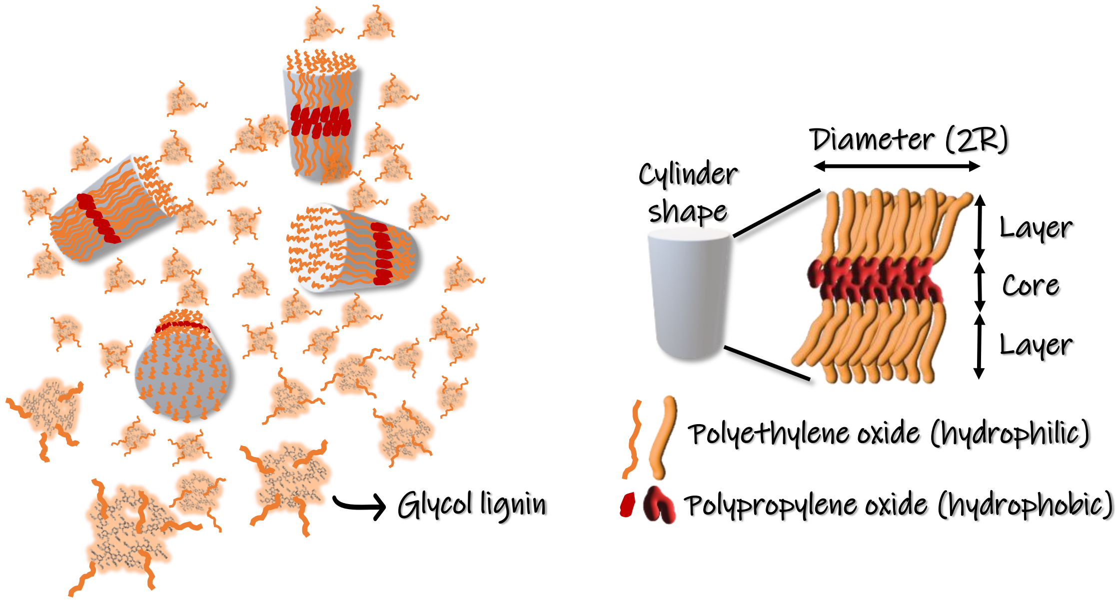

Fig. 4. Illustration on the formation of cylindrical surfactant assemblies in the presence of glycol lignin.

6.33 ×10^{10} cm^{-2}.[74] Our fitting resulted in a larger SLD for the hydrophobic core (4.16 × 10^{10} cm^{-2}), which may be attributed to the dense well-structured packing of the hydrophobic head, as suggested in other studies.[69] The size of the lamellar core that consists of the hydrophobic head can be related to the first peak of the pair distance distribution function (Fig. 3A inset), while the larger dimensions of the surfactant assembly (radius and thickness) can be associated with the neighboring peak(s). According to our model, the peaks of the scattering profile (Fig. 3A) at larger q values (0.1-1 nm^{-1}) are attributed to intraparticle scattering owing to the presence of the supramolecular assemblies.

Fig. 3B shows the SANS profiles recorded on the carbonized samples. For the microporous carbon obtained from glycol lignin, the decrease in intensity follows Porod's law, *i.e.*, the intensity decays with q^{-4}. This is due to the presence of graphitic layers and pores characterized by sharp density transitions (the neutron SLD for carbon can be taken as 6.15 × 10^{10} cm^{-2}).[76] The deviation from Porod's law becomes apparent at larger q values, which is a well-known phenomenon for microporous carbons owing to the presence of imperfectly stacked graphitic layers resulting in density fluctuations.[77,78] This deviation can be seen on the fitting results in Fig. S8.

The scattering profile obtained using the templated carbon (F/Gl/C 2/1/1) is markedly different from that of the microporous one (Fig. 3B). Our scattering profile resembles that of a mesoporous carbon, as reported by Mascotto et al.[76] By contrast matching the carbon using deuterated p-xylene, they could successfully separate the large mesoporous domain from other scattering contributions originating from micropores and small mesopores. The pair distance distribution function in Fig. 3B inset exhibits a broad asymmetric peak, which may indicate the presence of multiple pore populations (by size distribution). This consideration is further supported by our fitting results based on the unified model developed by Beaucage,[54-56] which resulted in a good fit when two structural levels were applied (Fig. S9). At both levels, the unified model includes a Guinier region at lower, and a power law regime at higher q values. The first structural level in our fitting captures the scattering profile in the high q range, yielding a radius of gyration (R_g) of 12 nm, and an exponent close to 4 for the power law regime following Porod's law, as expected. Fitting with a second structural level provided an R_g of 32 nm and an exponent of 3.2 indicating surface fractals. For simplicity, by assuming spherical pores according to Liu et al.,[79] the radius of the pores can be calculated by using the equation $r = \sqrt{5/3}\, R_g$. By doing so, we can arrive at an average radius of 16 nm and 41 nm, respectively, for the two scattering pore populations. These values are approximately in line with the pair distance distribution function in Fig. 3B inset, *i.e.*, the curve may be a result of overlapping peaks with centers at around 30 nm and 80 nm (pore size refers to the diameter here). The smaller average pore size (30 nm) is comparable to what we have obtained from the adsorption branch of the N_2 gas adsorption-desorption isotherm (Fig. 2B). It should be noted that due to the metastable nature of the adsorbed multilayer (no thermodynamic equilibrium), scattering experiments may provide a more quantitative information. It is also important to point out that SANS experiments probe "closed" pores as well, which cannot be accessed during gas adsorption measurements.

FE-SEM images on a templated carbon reveals further clues on the pre-existence of the cylindrical self-assemblies, as the well-structured black spots indicate in Fig. 5. Nevertheless, we need to stress that the structure is mostly disordered in line with the wide mesopore size distribution. A typical pore collapse can be seen in Fig. 5B inset, leading to a larger pore body.

Based on the textural analysis on the templated carbons, we chose the sample F/Gl/C

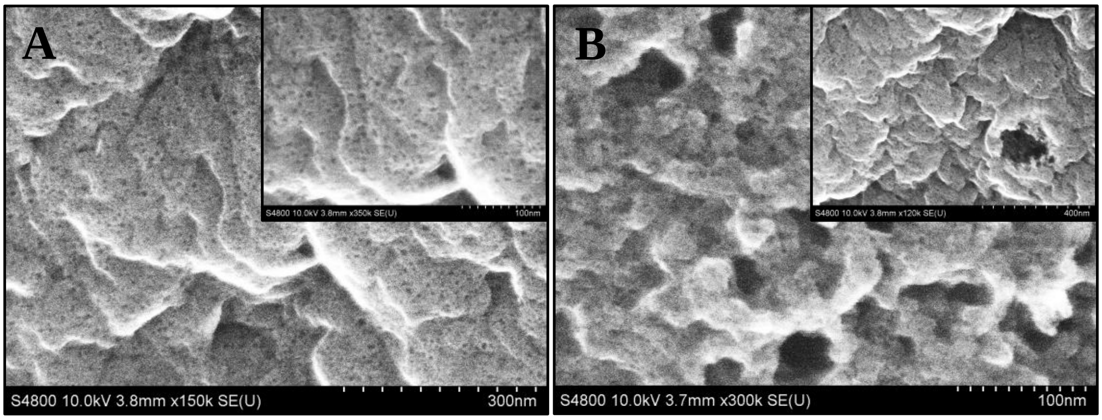

Fig. 5. (A,B) FE-SEM images recorded on a micro-mesoporous carbon sample prepared through soft-templating. (B) Inset shows a typical pore collapse, leading to a larger void.

2/1/1 for further CO_2 adsorption experiments, since this carbon is an almost purely micro-mesoporous material with well-defined, large mesopore volume (*i.e.*, a plateau is reached at high relative pressures, see Fig. 2A) among the samples.

3.3. High-pressure CO_2 adsorption

The CO_2 adsorption isotherms measured on the micro-mesoporous carbon (hereafter: large-pore mesoporous carbon) at different temperatures are shown in Fig. 6A (a zoom in on the low-pressure region can be found in Fig. S10). At low absolute pressures, the steep uptake of CO_2 can be associated with adsorption phenomena in micropores, while at higher pressures mesopore filling takes place.[80] The highest adsorption capacity was recorded as ~15 mmol g^{-1} at 270 K, at a pressure of around 3.1 MPa. At this temperature, the sharp increase in the adsorption amount above 3.0 MPa can be clearly attributed to capillary condensation in large mesopores. For the purely microporous carbon such phenomenon does not take place (Fig. S11). On account of the presence of the large mesopores, the maximum adsorption capacity is almost doubled compared to the purely microporous carbon (a maximum of 8.3 mmol g^{-1} at 270 K). Although less prevalent, such rapid increase in the adsorption amount can be noticed on the isotherms measured at 253 and 263 K as well, close to the saturation pressure, indicating capillary condensation. We could also observe hysteresis loops in these cases (Fig. S12), as we are operating below the hysteresis critical temperature (T_h), and above the hysteresis critical pore size under such conditions according to other studies that focus on CO_2 adsorption on nanoporous carbons.[25,81] In general, the hysteresis phenomenon depends on pore size

10.1002/cssc.202402034

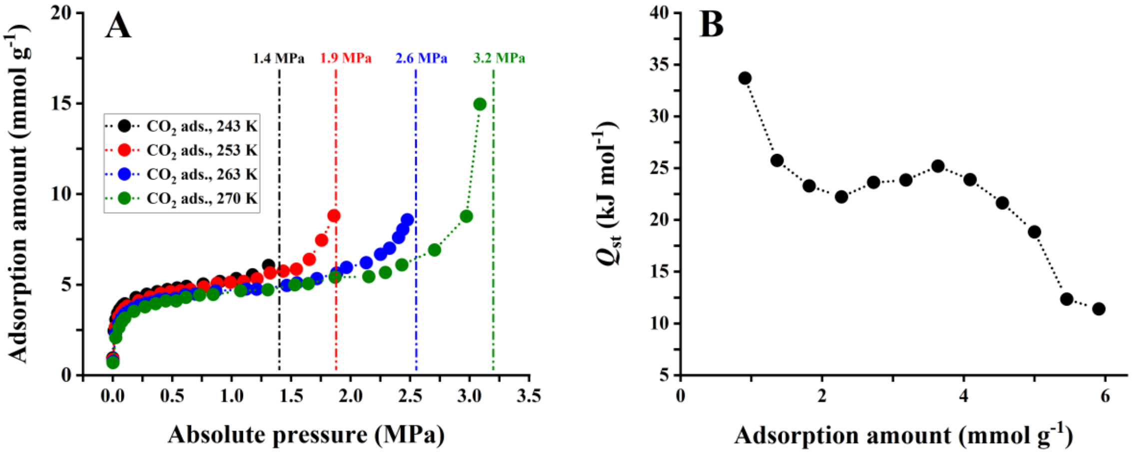

Fig. 6. (A) CO_2 adsorption isotherms measured at different temperatures (243-270 K) on the large-pore mesoporous carbon (F/Gl/C 2/1/1). Vertical dash-dotted lines indicate the saturation pressure at the given temperature. (B) Isosteric heat of adsorption (Q_{st}) derived from the isotherms, as a function of the adsorbed quantity. A zoom in on the low-pressure data points can be found in Fig. S10.

and temperature.[49] T_h is a subcritical temperature ($< T_c$) above which hysteresis vanishes, and reversible capillary condensation takes place up to the critical pore temperature (T_{cp}; and $T_h < T_{cp} < T_c$). In addition to this temperature dependence, capillary condensation occurs only in pores wider than a critical pore size (w_c), and hysteresis phenomenon is observable only above a certain pore width (w_h, and $w_c < w_h$). In our case at 270 K hysteresis loop is not visible anymore, reversible capillary condensation takes place (Fig. 7). Stefanopoulos et al.[25] observed hysteresis loops in the temperature range of 213-253 K for CMK-3 ordered mesoporous carbon, they assigned this phenomenon to the presence of large mesopores (“secondary pores” in their work, with sizes about 5-15 nm). In another work on CMK-3 by Dantas et al.,[81] a reversible capillary condensation was observed at 273 K. These observations are in line with our work, suggesting that 270 K is situated in the temperature regime above T_h for the given pore size. It is also known that the width of the hysteresis loop decreases with increasing temperature and decreasing pore size, and it eventually disappears at a critical pore size and temperature.[49,81] Such narrowing of the hysteresis loop with increasing temperature can be noticed when comparing the isotherms obtained at 253 and 263 K (Fig. S12).

At a given pressure, adsorption capacity decreases with increasing temperature (Fig. 6A and S10), indicating an exothermic process in line with other works on nanoporous carbons.[20-22] By using the Clausius-Clapeyron equation, we calculated the isosteric heat of adsorption (Q_{st}) as a measure of the strength of the adsorbent-adsorbate interactions. The calculated Q_{st} values, plotted against the amount of adsorbed CO_2 in Fig. 6B, fall within the range of physisorption (< 40 kJ mol^{-1}) indicating weak van der Waals type interactions.[9] The highest Q_{st} value amounts to 34 kJ mol^{-1} at the lowest CO_2 loading, in this region micropore filling takes place. The strength of physisorptive adsorption in micropores is known to be generally higher compared to larger mesopores due to the overlapping adsorption potentials of opposite pore walls;[49] this effect diminishes with increasing pore size, and therefore, Q_{st} generally decreases until monolayer saturation occurs.[58] At higher CO_2 loading, mesopore filling takes place with Q_{st} values ranging between ca. 20 and 25 kJ mol^{-1} (Fig. 6B). These values are close to those reported for other mesoporous carbons (small mesopores, ~5-10 nm; $Q_{st} \approx 17$-22 kJ mol^{-1}).[21,82] Variations in the Q_{st} values in this range may be attributed to variations in surface chemistry between groups of pores with different sizes. At a CO_2 uptake of around 5.5 mmol g^{-1}, Q_{st} decreases to a value that is close to the heat of condensation of CO_2 within our experimental temperature range.[13,83]

The excellence of our large-pore mesoporous carbon for CO_2 removal technologies (*e.g.*, for a pressure swing adsorption process) resides in the sharp reversible capillary condensation step observed at 270 K. To explain this further, we measured the CO_2 adsorption isotherm of a commercially available activated carbon (Shirasagi® WH5C) for comparison (Fig. 7). This benchmark reference sample is a microporous carbon with a reported specific surface area of 941 m^2 g^{-1}, and with a total pore volume of 0.68 cm^3 g^{-1}.[84] Although both the reference material and our sample have similar maximum CO_2 adsorption capacities, their adsorption-regeneration steps need markedly different energy inputs at high pressures. For example, in case of a pressure swing process, by taking advantage of the capillary condensation phenomenon, around 60% of the captured CO_2 could be recovered from our large-pore mesoporous carbon by decreasing the pressure from 3.1 MPa to 2.4 MPa (arrows indicate the pressure swing process in Fig. 7 with a target 60% CO_2 recovery). With the same pressure reduction, only ca. 14% of

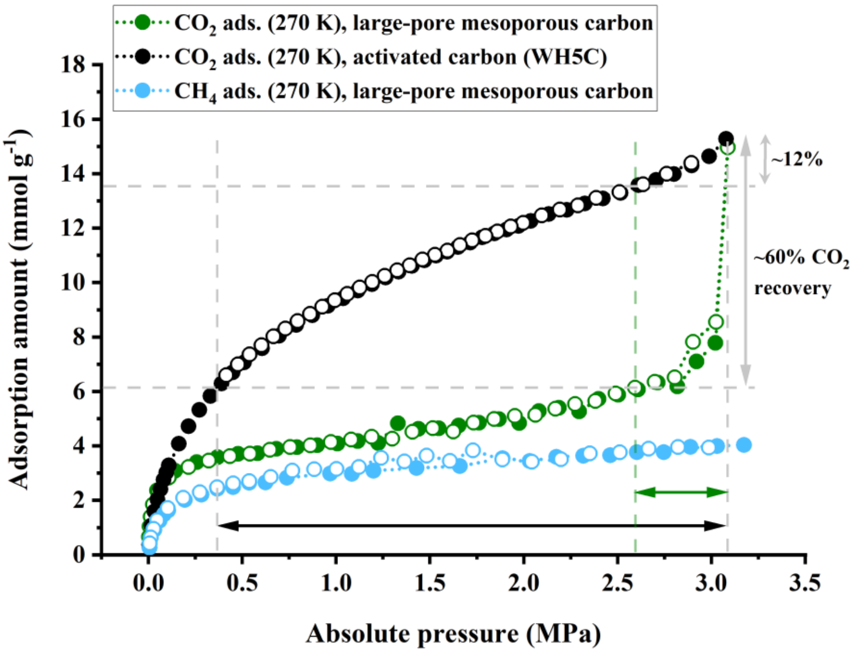

Fig. 7. CO_2 adsorption isotherms measured at 270 K on the large-pore mesoporous carbon (F/Gl/C 2/1/1), and on a reference commercial activated carbon sample. CH_4 adsorption isotherm (270 K) was obtained using the large-pore mesoporous carbon, for determining the CO_2/CH_4 selectivities. Desorption branches are shown with empty dots. Arrows indicate a pressure swing process operating with a target 60% adsorbed CO_2 recovery.

the adsorbed CO_2 can be released from the commercial activated carbon. In fact, the pressure needs to be reduced below 0.5 MPa to recover around 60% of the adsorbed CO_2 in the latter case, highlighting the superiority of our large-pore mesoporous carbon for a cost-effective pressure swing operation. Our material shows outstanding cycling performance as well, even under high pressure and low temperature conditions we did not notice appreciable performance change within reasonable deviations (Fig. S13). Even after several cycles and various experiments, well identifiable hysteresis loop appears at 253 K, indicating the robust nature of the material.

It should be noted, however, that much higher adsorption amounts can be achieved by preparing activated carbons with drastically higher surface areas and pore volumes. Among the highest reported CO_2 adsorption capacities on nanoporous carbons in high pressure regimes are those reported by Singh et.[22] (and related publications).[21] They prepared activated mesoporous carbons with small pore size (< 6 nm), extremely high specific surface areas (up to ~3600 $m^2\ g^{-1}$) and pore volumes (up to 2.16 $cm^3\ g^{-1}$), reaching a CO_2 adsorption capacity of 39.1 mmol g^{-1} at 273 K and 3 MPa absolute pressure. Furthermore, Canevesi et al.[85] for an activated micro-mesoporous carbon (pore size < 3 nm) with a specific surface area of 3200 m^2 g^{-1} and a pore volume of 1.65 cm^3 g^{-1} achieved an adsorption capacity of ~37 mmol g^{-1} under similar conditions (273 K, 3 MPa). Although these materials can be attractive for certain scenarios, our material may offer a promising alternative for a low-temperature high-pressure PSA process with excellent CO_2 desorption profile per unit pressure within the capillary condensation regime. This means that the large-pore mesoporous carbon prepared herein can offer an energy-efficient CO_2 capture-and-release option, while still demonstrating a reasonably high adsorption capacity under such conditions. We should also note that at present our material has somewhat limited pore volume (0.15 cm^3 g^{-1} mesopore volume) compared to other templated large-pore mesoporous carbons. For example, by synthesizing customized large block copolymer templates, such as poly(ethylene oxide)-*block*-poly(styrene), large-pore ordered mesoporous carbons with pore sizes of 12-33 nm, and pore volumes as large as 0.7 cm^3 g^{-1} have been reported.[86] Similarly large pore sizes (~9-22 nm) and pore volumes (up to ~0.8 cm^3 g^{-1}) have been realized using poly(methyl methacrylate) as the hydrophobic segment of the diblock copolymer.[87] Even higher pore volumes may be achieved using hard templating methods, for example Vorokhta et al.[20] disclosed a mesopore volume of 3.4 cm^3 g^{-1} for a relatively large-pore (with 14-15 nm diameters) ordered mesoporous carbon. The kind of large-pore mesoporous carbon developed in the present work offers enormous future opportunities, as there is still much room for further increasing the CO_2 uptake in light of these previous reports.

To further highlight the merit of the large-pore mesoporous carbon for CO_2 removal from natural gas streams under high pressures, we measured the adsorption isotherm for CH_4 (Fig. 7). We calculated the selectivities for equimolar CO_2/CH_4 mixtures. The CO_2/CH_4 selectivity (S_{CO_2/CH_4}, mol/mol) increases with increasing pressure at 270 K, values of 1.5, 1.7, 2.8 and 3.7 were calculated at pressures of 1.0, 2.0, 3.0 and 3.1 MPa, respectively. The preferential adsorption of CO_2 over CH_4 on carbon surfaces can be understood in light of polarizability differences: while CH_4 is a symmetric nonpolar molecule, CO_2 has a quadrupole moment of 13.4×10^{-40} cm^2 promoting stronger van der Waals interactions.[59] For comparison, lower S_{CO_2/CH_4} (~2) can be realized for the activated carbon shown in Fig. 7 close to the saturation pressure (3.1 MPa) at 270 K, as reported in one of our previous works.[13] The selectivity difference close to the saturation pressure (3 MPa) is almost 2-fold in favor of our large-pore mesoporous carbon owing to the capillary condensation phenomenon of CO_2 that takes place in large mesopores. To relate these values with other studies, by using the IAST method with the Sips adsorption model, an S_{CO_2/CH_4} of ~7 was reported for 50 vol% CO_2 using a microporous carbon (specific surface area of 905 m^2 g^{-1}, total pore volume of 0.27 cm^3 g^{-1}) at somewhat higher temperature (298 K), at around 3 MPa.[59] A single gas CO_2 and CH_4 adsorption capacity of ~6 mmol g^{-1} and ~3.5 mmol g^{-1}, respectively, was measured for this material under the same conditions.

4. Conclusions

The widespread implementation of carbon capture and utilization technologies heavily relies on the development of affordable, negative-carbon materials that not only effectively capture large amount of CO_2 per unit mass, but can be readily regenerated through economically viable, cost-effective means. CO_2 removal scenarios under extreme operating conditions, such as high-pressure regimes during natural gas processing, pose further challenges with a limited palette of material choices. In this work, we realized a unique large-pore mesoporous carbon from a templated technical lignin (PEG-grafted lignin, coined as glycol lignin) for the first time. This material exhibited excellent energy-efficient CO_2 capture-and-release capabilities and improved CO_2/CH_4 selectivity at high pressure compared to a benchmark activated carbon, on account of capillary condensation close to the saturation pressure at 270 K. Through small angle neutron scattering experiments, we shed light on the presence of peculiar supramolecular assemblies in the templated polymeric material, distinct from other lignin-based systems. Such nanostructuration can be attributed to the similar hydrophilic PEG structural motifs on both the template and the biopolymer. Our study provides novel means for fabricating advanced lignin-based nanoarchitectures, and further proposes large-pore mesoporous carbons as excellent platforms for the development of cost-efficient CO_2 removal technologies operating under high pressure and low temperature environment.

Supporting Information

Supporting Information is available from the Wiley Online Library or from the authors.

Acknowledgements

L. Szabó would like to thank for the start-up grant provided by the Forestry and Forest Products Research Institute. The work described here received support from the Ministry of Agriculture, Forestry and Fisheries (Japan) under Grant Number J008722 with the title "Development of Glycol Lignin-Based High-Value-Added Materials". This work was also partially supported by JSPS KAKENHI (Grant Number 24K01409). Access to the experiment at SANS-J (C3-2) was provided by the Japan Research Reactor-3 (JRR-3) with the approval of the Japan Atomic Energy Agency (JAEA; Proposal 2024-D1050).

Conflict of interests

The authors declare no conflict of interest.

References

[1] M. Bui, C. S. Adjiman, A. Bardow, A. Boston, S. Brown, E. J. Anthony, P. S. Fennell, S. Fuss, A. Galindo, L. A. Hackett, J. P. Hallett, H. J. Herzog, G. Jackson, J. Kemper, S. Krevor, G. C. Maitland, M. Matuszewski, I. S. Metcalfe, C. Petit, G. Puxty, J. Reimer, D. M. Reiner, E. S. Rubin, S. A. Scott, N. Shah, B. Smit, J. P. M. Trusler, P. Webley, J. Wilcox, N. M. Dowell, *Energy Environ. Sci.* **2018**, *11*, 1062.

[2] C. Wu, Q. Huang, Z. Xu, A. T. Sipra, N. Gao, L. P. de Souza Vandenberghe, S. Vieira, C. R. Soccol, R. Zhao, S. Deng, S. K. S. Boetcher, S. Lu, H. Shi, D. Zhao, Y. Xing, Y. Chen, J. Zhu, D. Feng, Y. Zhang, L. Deng, G. Hu, P. A. Webley, D. Liang, Z. Ba, A. Mlonka-Mędrala, A. Magdziarz, N. Miskolczi, Sz. Tomasek, S. S. Lam, S. Y. Foong, H. S. Ng, L. Jiang, X. Yan, Y. Liu, Y. Ji, H. Sun, Y. Zhang, H. Yang, X. Zhang, M. Sun, D. C. W. Tsang, J. Shang, C. Muller, M. Rekhtina, M. Krödel, A. H. Bork, F. Donat, L. Liu, X. Jin, W. Liu, S. Saqline, X. Wu, Y. Xu, A. L. Khan, Z. Ali, H. Lin, L. Hu, J. Huang, R. Singh, K. Wang, X. He, Z. Dai, S. Yi, A. Konist, M. H. S. Baqain, Y. Zhao, S. Sun, G. Chen, X. Tu, A. Weidenkaff, S. Kawi, K. H. Lim, C. Song, Q. Yang, Z. Zhao, X. Gao, X. Jiang, H. Ji, T. E. Akinola, A. Lawal, O. S. Otitoju, M. Wang, G. Zhang, L. Ma, B. C. Sempuga, X. Liu, E. Oko, M. Daramola, Z. Yu, S. Chen,

G. Kang, Q. Li, L. Gao, L. Liu, H. Zhou, *Carbon Capture Sci. Technol.* **2024**, *11*, 100178.

[3] H. Mao, J. Tang, G. S. Day, Y. Peng, H. Wang, X. Xiao, Y. Yang, Y. Jiang, S. Chen, D. M. Halat, A. Lund, X. Lv, W. Zhang, C. Yang, Z. Lin, H.-C. Zhou, A. Pines, Y. Cui, J. A. Reimer, *Sci. Adv.* **2022**, *8*, eabo6849.

[4] T. Wilberforce, A. G. Olabi, E. T. Sayed, K. Elsaid, M. A. Abdelkareem, *Sci. Total Environ.* **2021**, *761*, 143203.

[5] G. T. Rochelle, *Science* **2009**, *325*, 1652.

[6] C. Gouedard, D. Picq, F. Launay, P.-L. Carrette, *Int. J. Greenh. Gas Control.* **2012**, *10*, 244.

[7] D. M. D'Alessandro, B. Smit, J. R. Long, *Angew. Chem. Int. Ed.* **2010**, *49*, 6058.

[8] R. L. Siegelman, E. J. Kim, J. R. Long, *Nat. Mater.* **2021**, *20*, 1060.

[9] H. A. Patel, S. H. Je, J. Park, D. P. Chen, Y. Jung, C. T. Yavuz, A. Coskun, *Nature Commun.* **2013**, *4*, 1357.

[10] J.-B. Lin, T. T. T. Nguyen, R. Vaidhyanathan, J. Burner, J. M. Taylor, H. Durekova, F. Akhtar, R. K. Mah, O. Ghaffari-Nik, S. Marx, N. Fylstra, S. S. Iremonger, K. W. Dawson, P. Sarkar, P. Hovington, A. Rajendran, T. K. Woo, G. K. H. Shimizu, *Science* **2021**, *374*, 1464.

[11] Y. Zhou, J. Zhang, L. Wang, X. Cui, X. Liu, S. S. Wong, H. An, N. Yan, J. Xie, C. Yu, P. Zhang, Y. Du, S. Xi, L. Zheng, X. Cao, Y. Wu, Y. Wang, C. Wang, H. Wen, L. Chen, H. Xing, J. Wang, *Science* **2021**, *373*, 315.

[12] G. Durá, V. L. Budarin, J. A. Castro-Osma, P. S. Shuttleworth, S. C. Y. Quek, J. H. Clark, M. North, *Angew. Chem. Int. Ed.* **2016**, *128*, 9319.

[13] M. Inoue, E. Ismail, S. Samitsu, H. Kanoh, I. Ichinose, *Chem. Lett.* **2022**, *51*, 1113.

[14] H. Lin, J. Lu, A. M. Abed, K. Nag, M. Fayed, A. Deifalla, A. S. Bin Mahfouz, A. M. Galal, *Chemosphere* **2023**, *329*, 138583.

[15] T. E. Rufford, S. Smart, G. C. Y. Watson, B. F. Graham, J. Boxall, J. C. D. da Costa, E. F. May, *J. Pet. Sci. Eng.* **2012**, *94-95*, 123.

[16] E. J. Kim, R. L. Siegelman, H. Z. H. Jiang, A. C. Forse, J.-H. Lee, J. D. Martell, P. J. Milner, J. M. Falkowski, J. B. Neaton, J. A. Reimer, S. C. Weston, J. R. Long, *Science* **2020**, *369*, 392.

[17] R. Ben-Mansour, M. A. Habib, O. E. Bamidele, M. Basha, N. A. A. Qasem, A. Peedikakkal, T. Laoui, M. Ali, *Appl. Energy* **2016**, *161*, 225.

[18] H. Lin, J. Lu, A. M. Abed, K. Nag, M. Fayed, A. Deifalla, A. S. Bin Mahfouz, A. M. Galal, *Chemosphere* **2023**, *329*, 138583.

[19] A. Aspelund, M. J. Mølnvik, G. De Koeijer, *Chem. Eng. Res. Des.* **2006**, *84*, 847.

[20] M. Vorokhta, J. Morávková, D. Řimnáčová, R. Pilař, A. Zhigunov, M. Švábová, P. Sazama, *J. CO_2 Util.* **2019**, *31*, 124.

[21] G. Singh, K. S. Lakhi, I. Y. Kim, S. Kim, P. Srivastava, R. Naidu, A. Vinu, *ACS Appl. Mater. Interfaces* **2017**, *9*, 29782.

[22] G. Singh, K. S. Lakhi, CI Sathish, K. Ramadass, J.-H. Yang, A. Vinu, *ACS Appl. Nano Mater.* **2019**, *2*, 1604.

[23] L. Zhou, X. Liu, J. Li, N. Wang, Z. Wang, Y. Zhou, *Chem. Phys. Lett.* **2005**, *413*, 6.

[24] G. Chandrasekar, W.-J. Son, W.-S. Ahn, *J. Porous Mater.* **2009**, *16*, 545.

[25] K. L. Stefanopoulos, C. Tampaxis, A. A. Sapalidis, F. K. Katsaros, T. G. A. Youngs, D. T. Bowron, T. A. Steriotis, *Carbon* **2020**, *167*, 296.

[26] C. Liang, Z. Li, S. Dai, *Angew. Chem. Int. Ed.* **2008**, *47*, 3696.

[27] T.-Y. Ma, L. Liu, Z.-Y. Yuan, *Chem. Soc. Rev.* **2013**, *42*, 3977.

[28] L. Chuenchom, R. Kraehnert, B. M. Smarsly, *Soft Matt.* **2012**, *8*, 10801.

[29] L. Szabó, W. Thielemans, J. W. Seo, F. Buysschaert, D. D. Dionysiou, V. Vandeginste, *RSC Sustain.* **2023**, *1*, 1354.

[30] Y. Deng, J. Wei, Z. Sun, D. Zhao, *Chem. Soc. Rev.* **2013**, *42*, 4054.

[31] J. Wei, Z. Sun, W. Luo, Y. Li, A. A. Elzatahry, A. M. Al-Enizi, Y. Deng, D. Zhao, *J. Am. Chem. Soc.* **2017**, *139*, 1706.

[32] M. S. Khosrowshahi, H. Mashhadimoslem, H. Shayesteh, G. Singh, E. Khakpour, X. Guan, M. Rahimi, F. Maleki, P. Kumar, A. Vinu, *Adv. Sci.* **2023**, *10*, 2304289.

[33] D. Torres, S. Pérez-Rodríguez, L. Cesari, C. Castel, E. Favre, V. Fierro, A. Celzard, *Carbon* **2021**, *183*, 12.

[34] S. Chatterjee, T. Saito, *ChemSusChem* **2015**, *8*, 3941.

[35] K. Chen, Z.-J. He, Z.-H. Liu, A. J. Ragauskas, B.-Z. Li, Y.-J. Yuan, *ChemSusChem* **2022**, *15*, e202201284.

[36] V. García-Negrón, S. C. Chmely, J. Ilavsky, D. J. Keffer, D. P. Harper, *ACS Sustainable Chem. Eng.* **2022**, *10*, 1786.

[37] R. Madhu, A. P. Periasamy, P. Schlee, S. Hérou, M.-M. Titirici, *Carbon* **2023**, *207*, 172.

[38] D. Saha, Y. Li, Z. Bi, J. Chen, J. K. Keum, D. K. Hensley, H. A. Grappe, H. M. Meyer, III, S. Dai, M. P. Paranthaman, A. K. Naskar, *Langmuir* **2014**, *30*, 900.

[39] S. Herou, M. C. Ribadeneyra, R. Madhu, V. Araullo-Peters, A. Jensen, P. Schlee, M. Titirici, *Green Chem.* **2019**, *21*, 550.

[40] C. Glatthaar, M. Wang, L. Q. Wagner, F. Breckwoldt, Z. Guo, K. Zheng, M. Kriechbaum, H. Amenitsch, M.-M. Titrici, B. M. Smarsly, *Chem. Mater.* **2023**, *35*, 10416.

[41] X. Wang, M. Qiu, R. L. Smith, J. Wang, F. Shen, X. Qi, *ACS Sustainable Chem. Eng.* **2020**, *8*, 18157.

[42] X. Wang, X. Liu, R. L. Smith, Y. Liang, X Qi, *Green Chem.* **2021**, *23*, 8632.

[43] F. L. Braghiroli, V. Fierro, J. Parmentier, A. Pasc, A. Celzard, *Green Chem.* **2016**, *18*, 3265.

[44] J. Castro-Gutiérrez, A. Sanchez-Sanchez, J. Ghanbaja, N. Díez, M. Sevilla, A. Celzard, V. Fierro, *Green Chem.* **2018**, *20*, 5123.

[45] T. T. Nge, Y. Tobimatsu, S. Takahashi, E. Takata, M. Yamamura, Y. Miyagawa, T. Ikeda, T. Umezawa, T. Yamada, *ACS Sustainable Chem. Eng.* **2018**, *6*, 7841.

[46] T. T. Nge, T. Yamada, Y. Tobimatsu, M. Yamamura, R. Ishii, O. Tanaike, T. Ebina, *ACS Sustainable Chem. Eng.* **2021**, *9*, 756.

[47] T. T. Nge, E. Takata, S. Takahashi, T. Yamada, *ACS Sustainable Chem. Eng.* **2016**, *4*, 2861.

[48] F. Ambroz, T. J. Macdonald, V. Martis, I. P. Parkin, *Small Methods* **2018**, *2*, 1800173.

[49] S. Lowell, J. E. Shields, M. A. Thomas, M. Thommes, *Characterization of Porous Solids and Powders: Surface Area, Pore Size and Density*, Springer Science+Business Media, New York, NY 2004.

[50] M. Thommes, K. Kaneko, A. V. Neimark, J. P. Olivier, F. Rodriguez-Reinoso, J. Rouquerol, K. S. W. Sing, *Pure Appl. Chem.* **2015**, *87*, 1051.

[51] T. Kumada, R. Motokawa, H. Iwase, *J. Appl. Crystallogr.* **2024**, *57*, 728.

[52] T. Kumada, R. Motokawa, Y. Oba, H. Nakagawa, Y. Sekine, C. Micheau, Y. Ueda, T. Sugita, A. Birumachi, M. Sasaki, K. Hiroi, H. Iwase, *J. Appl. Crystallogr.* **2023**, *56*, 1776.

[53] J. Ilavsky, P. R. Jemian, *J. Appl. Cryst.* **2009**, *2*, 347.

[54] G. Beaucage, *J. Appl. Cryst.* **1995**, *28*, 717.

[55] G. Beaucage, *J. Appl. Cryst.* **1996**, *29*, 134.

[56] B. Hammouda, *J. Appl. Cryst.* **2010**, *43*, 1474.

[57] M. Doucet, J. H. Cho, G. Alina, Z. Attala, J. Bakker, P. Beaucage, W. Bouwman, R. Bourne, P. Butler, I. Cadwallader-Jones, K. Campbell, T. Cooper-Benun, C. Durniak, L. Forster, P. Gilbert, M. Gonzalez, R. Heenan, A. Jackson, S. King, C. Wolf, SasView version 5.0.6, Zenodo, 2023, https://doi.org/10.5281/zenodo.7581379

[58] P. Halder, M. Maurya, S. K. Jain, J. K. Singh, *Phys. Chem. Chem. Phys.* **2016**, *18*, 14007.

[59] G. Greco, R. L. S. Canevesi, C. Di Stasi, A. Celzard, V. Fierro, J. J. Manyà, *Renew. Energy* **2022**, *191*, 122.

[60] S. A. Nicolae, P. Á. Szilágyi, M. M. Titirici, *Carbon* **2020**, *169*, 193.

[61] J. Brinker, Y. Lu, A. Sellinger, H. Fan, *Adv. Mater.* **1999**, *11*, 579.

[62] K. S. W. Sing, R. T. Williams, *Adsorp. Sci. Technol.* **2004**, *22*, 773.

[63] Q. K. Loi, S. J. Tan, D. D. Do, D. Nicholson, *Ind. Eng. Chem. Res.* **2021**, *60*, 15343.

[64] K. A. Cychosz, R. Guillet-Nicolas, J. García-Martínez, M. Thommes, *Chem. Soc. Rev.* **2017**, *46*, 389.

[65] J. Castro-Gutiérrez, N. Díez, M. Sevilla, M. T. Izquierdo, A. Celzard, V. Fierro, *Renew. Sustain. Energy Rev.* **2021**, *151*, 111600.

[66] J. Castro-Gutiérrez, J. Jagiello, A. Celzard, V. Fierro, *Chem. Eng. J.* **2024**, *497*, 154938.

[67] S. Kubo, R. J. White, N. Yoshizawa, M. Antonietti, M.-M. Titirici, *Chem. Mater.* **2011**, *23*, 4882.

[68] A. Rajbanshi, M. A. Da Silva, N. Mahmoudi, A. Janeczek, A. Shaw, J. Dawson, M. T. Cook, *Soft Matter* **2024**, *20*, 103.

[69] C. Wu, T. Liu, B. Chu, D. K. Schneider, V. Graziano, *Macromolecules* **1997**, *30*, 4574.

[70] A. P. Constantinou, V. Nele, J. J. Doutch, J. S. Correia, R. M. Moiseev, M. Cihova, D. C. A. Gaboriau, J. Krell, V. V. Khutoryanskiy, M. M. Stevens, T. K. Georgiou, *Macromolecules* **2022**, *55*, 1783.

[71] Y. Li, T. Shi, Z. Sun, L. An, Q. Huang, *J. Phys. Chem. B* **2006**, *110*, 26424.

[72] K. Mortensen, Y. Talmon, *Macromolecules* **1995**, *28*, 8829.

[73] J. Jiang, C. Burger, C. Li, J. Li, M. Y. Lin, R. H. Colby, M. H. Rafailovich, J. C. Sokolov, *Macromolecules* **2007**, *40*, 4016.

[74] M. Martínez-Sanz, M. J. Gidley, E. P. Gilbert, *Carbohydr. Polym.* **2015**, *125*, 120.

[75] I. Grillo, I. Morfin, S. Prévost, *Langmuir* **2018**, *34*, 13395.

[76] S. Mascotto, D. Kuzmicz, D. Wallacher, M. Siebenbürger, D. Clemens, S. Risse, J. Yuan, M. Antonietti, M. Ballauff, *Carbon* **2015**, *82*, 425.

[77] W. Ruland, *Carbon* **2001**, *39*, 323.

[78] L. Szabó, X. Xu, K. Uto, J. Henzie, Y. Yamauchi, I. Ichinose, M. Ebara, *ACS Appl. Mater. Interfaces* **2022**, *14*, 4004.

[79] Y. Liu, M. Paskevicius, M. V. Sofianos, G. Parkinson, C.-Z. Li, *Carbon* **2021**, *172*, 454.

[80] X. Hu, M. Radosz, K. A. Cychosz, M. Thommes, *Environ. Sci. Technol.* **2011**, *45*, 7068.

[81] S. Dantas, K. C. Struckhoff, M. Thommes, A. V. Neimark, *Langmuir* **2019**, *35*, 11291.

[82] K. S. Lakhi, W. S. Cha, J.-H. Choy, M. Al-Ejji, A. M. Abdullah, A. M. Al-Enizi, A. Vinu, *Microporous Mesoporous Mater.* **2016**, *233*, 44.

[83] S. Martynov, S. Brown, H. Mahgerefteh, *Greenhouse Gas Sci. Technol.* **2013**, *3*, 136.

[84] A. Miura, E. Shiratani, I. Yoshinaga, T. Hitomi, K. Hamada, K. Takaki, *JARQ* **2008**, *42*, 49.

[85] R. L. S. Canevesi, S. Schaefer, M. T. Izquierdo, A. Celzard, V. Fierro, *ACS Appl. Nano Mater.* **2022**, *5*, 3843.

[86] Y. Deng, Y. Cai, Z. Sun, D. Gu, J. Wei, W. Li, X. Guo, J. Yang, D. Zhao, *Adv. Funct. Mater.* **2010**, *20*, 3658.

[87] J. Wei, Y. Deng, J. Zhang, Z. Sun, B. Tu, D. Zhao, *Solid State Sci.* **2011**, *13*, 784.

A large-pore mesoporous carbon is prepared from a wood-derived templated technical lignin. Nanoconfinement-induced capillary condensation of CO_2 occurs in large mesopores, leading to an energy-efficient pressure swing CO_2 capture-and-release process. This phenomenon unlocks untapped opportunities for CO_2 separations with cost-effective regeneration options.

L. Szabó,* M. Inoue, Y. Sekine, R. Motokawa, Y. Matsumoto, T. T. Nge, E. Ismail, I. Ichinose,* T. Yamada*

Nanoconfinement-Driven Energy-Efficient CO_2 Capture and Release at High Pressures on a Unique Large-Pore Mesoporous Carbon